nanomaterials

MDPI

Article

Defect Engineering Enhances the Charge Separation of CeO_2 Nanorods toward Photocatalytic Methyl Blue Oxidation

Jindong Yang [1], Ning Xie [2,3], Jingnan Zhang [1], Wenjie Fan [4], Yongchao Huang [2,3,*] and Yexiang Tong [1,*]

1 MOE Laboratory of Bioinorganic and Synthetic Chemistry the Key Lab of Low-Carbon Chemistry and Energy Conservation of Guangdong Province, School of Chemistry, Sun Yat-sen University, Guangzhou 510006, China; usayjd@hotmail.com (J.Y.); zhangjn28@mail2.sysu.edu.cn (J.Z.)

2 Institute of Environmental Research at Greater Bay Area, Key Laboratory for Water Quality and Conservation of the Pearl River Delta, Ministry of Education, Guangzhou 510006, China; xiening0101@163.com

3 Guangzhou Key Laboratory for Clean Energy and Materials, Guangzhou University, Guangzhou 510006, China

4 Analysis and Testing Center, South China Normal University, Guangzhou 510006, China; 20175033@m.scnu.edu.cn

* Correspondence: huangych@gzhu.edu.cn (Y.H.); chedhx@mail.sysu.edu.cn (Y.T.)

Received: 1 November 2020; Accepted: 18 November 2020; Published: 21 November 2020

Abstract: Defect-rich photocatalytic materials with excellent charge transfer properties are very popular. Herein, Sm-doped CeO_2 nanorods were annealed in a N_2 atmosphere to obtain the defective Sm-doped CeO_2 photocatalysts (Vo–Sm–CeO_2). The morphology and structure of Vo–Sm–CeO_2 were systematically characterized. The Vo–Sm–CeO_2 nanorods demonstrated an excellent photodegradation performance of methyl blue under visible light irradiation compared to CeO_2 nanorods and Sm–CeO_2. Reactive oxygen species including OH, $\cdot O_2^-$, and h^+ were confirmed to play a pivotal role in the removal of pollutants via electron spin resonance spectroscopy. Doping Sm enhances the conductivity of CeO_2 nanorods, benefiting photogenerated electrons being removed from the surface reactive sites, resulting in the superior performance.

Keywords: cerium oxide; Sm doping; defects; environmental photocatalysis; nanomaterials

1. Introduction

Semiconductor-based photocatalytic oxidation reactions have been extensively considered as promising advanced oxidation processes (AOPS) technology for the removal of pollutants in the air and water that have a negative impact on environmental quality, ecosystem safety, and human health [1–11]. However, low photocatalytic efficiency limits its practical application. Thus, various works have been developed to improve its photocatalytic performance via enhanced light absorption and increased the separation efficiency of photogenerated charge carriers [12–15]. Among them, defect engineering is an efficient method to prepare the ideal photocatalysts [16,17].

Crystallographic defects are generated in materials when the neat arrangement of atoms is broken [18–21]. At present, defects are mainly prepared by the following methods: hydrogen reduction, calcining under nitrogen atmosphere, strong reducing agent reduction, electric reduction, etc. [22–24]. The defects in photocatalysts not only act as recombination centers for free electrons and holes, but also scattering centers for electron and hole travelling, which is not conducive to the diffusion of charge carriers [25–28]. Defects on the surface of semiconductors can be reactive sites where photoelectrons reduce dissolved O_2 to O_2^- [29]. Electron trapping sites can consume the photoelectrons,

thus preventing the recombination of charge carriers, which can enhance the photocatalytic performance [30,31]. However, the instability of defective materials limits its application because O_2 gases will refill the defect sites. Therefore, how to use defects effectively to improve the performance and stability of catalysts is one of the research hotspots at present.

Cerium oxide (CeO_2) has attracted attention in many research fields such as photocatalysis, thermo-catalysis, and electro-catalysis due to its remarkable oxygen-storage ability and redox properties (Ce^{4+}/Ce^{3+}) [32–37]. These properties enhance the release of active oxygen species, balancing the nascent electric charges spontaneously, resulting in defects in CeO_2 forming and being eliminated quickly [38,39]. Aslam et al. prepared CeO_{2-x} surface defects and used them for the degradation of phenol and its derivatives. Defects serve as the traps and transfer centers to enhance the generation of reactive oxygen species [40]. Jiang and coworkers confirmed the surface-defect dependence of photo-performance [39]. Furthermore, doping a trivalent element into CeO_2 introduces defects such as Eu-doped CeO_2 and Yb-CeO_2 [41–44]. Our reported work demonstrated that Eu doping can introduce oxygen vacancies into CeO_2 nanosheets, enhancing the charge transfer. This phenomenon has inspired us to propose enhancing the oxidation and reduction properties and introducing surface defects to improve the photocatalytic performance of CeO_2.

In this work, we prepared the defective Ce-based photocatalysts (Vo–Sm–CeO_2) where Sm-doped CeO_2 nanorods were annealed in a N_2 atmosphere (Figure 1a). The defects in CeO_2 were systematically characterized by electron spin resonance (EPR), X-ray photoelectron spectroscopy (XPS), and Raman. The Vo–Sm–CeO_2 nanorods were tested for the photodegradation of methyl blue (MB) and the results revealed that the photocatalytic activity of Vo–Sm–CeO_2 was higher than those of pristine CeO_2 and Sm-doped CeO_2, which can be attributed to the existence of defects in CeO_2. Defects in CeO_2 nanorods enhanced the electrical conduction and promoted charge transfer dynamics. Moreover, the role of defects in producing reactive oxygen species (ROS) was also studied by electron spin resonance spectroscopy.

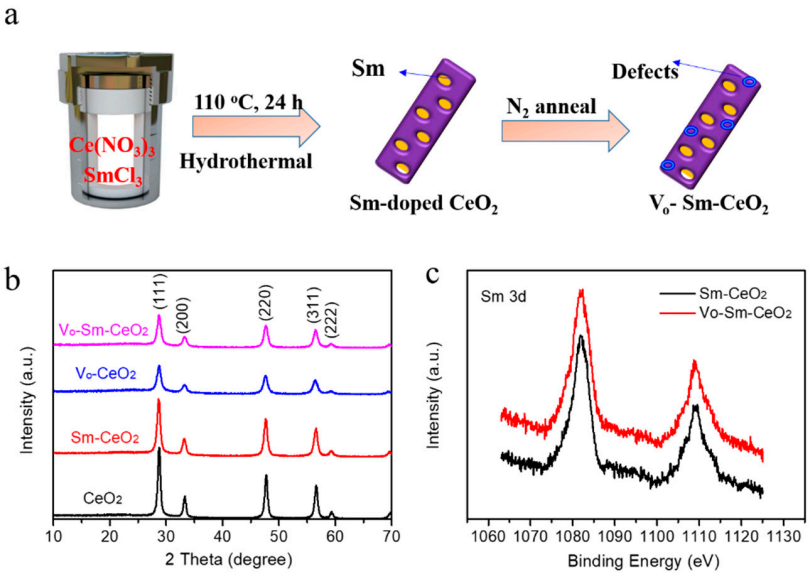

Figure 1. (**a**) Sketch map for preparing Vo–Sm–CeO_2 sample. (**b**) XRD spectra of CeO_2, Sm–CeO_2, Vo–CeO_2 and Vo–Sm–CeO_2. (**c**) Sm 3d XPS spectra of Sm–CeO_2 and Vo–Sm–CeO_2.

2. Experimental Section

2.1. Preparation of Photocatalysts

CeO_2 was obtained by the following method. $Ce(NO_3)_3$ $6H_2O$ was dissolved in distilled water (5 mL). Then, 10 mL of 14 M NaOH was added into the above solution. Finally, the solution was transferred into a Teflon-lined stainless-steel autoclave and it was kept at 110 °C for 24 h. The obtained

solid was washed with water and calcined in air at 200 °C for 1 h. Sm doped-CeO_2 was obtained with the same CeO_2 nanorods by adding 0.13 g, 0.26 g, and 0.39 g $SmCl_3$, respectively. CeO_2 and Sm–CeO_2 were annealed in N_2 gas at 600 °C for 4 h with a ramp rate of 10 °C min^{-1} to obtain Vo–CeO_2 and Vo–Sm–CeO_2, respectively. The 2.0 g prepared samples were put into a tube furnace (OTF-1500X-II corundum tube ø 60 mm by Hefei Kejing Materials Technology Co. Ltd., Hefei, China), and the flow rate of N_2 was continuously pumped into the tube for 30 min at a flow rate of 300 mL min^{-1}. The purpose was to drain the air out of the tube and form a high concentration of N_2 atmosphere in the tube. A flow controller (Beijing Sevenstar Flow Co. Ltd., Beijing, China) was used to maintain the flow stability of N_2.

2.2. Characterization of Photocatalysts

The main instruments used in the experiment are listed as follows: transmission electron microscope (JEM2010-HR, Tokyo, Japan), scanning electron microscope (Gemini SEM 500, Jena, Germany), X-ray diffractometer (D8 ADVANCE, NASDAQ, Billerica, MA, USA), UV−Vis−NIR spectrophotometer (UV-2450, Shimadzu, China), X-ray photoelectron spectroscope (ESCALAB250, Waltham, MA, USA), specific surface area measurements (ASAP 2020V3.03H, Waltham, MA, USA), Raman (Nicolet NXR 9650, Waltham, MA, USA), and a room-temperature photoluminescence spectroscope (FLS920, Edinburgh, UK). The electrochemical tests were carried out with a CHI 660C electrochemical station in a standard three electrode configuration. The illumination source was an AM 1.5 G solar simulator (Newport, LCS 100 94011A (class A), Waltham, MA, USA) directed at the quartz PEC cell (100 mW cm^2). The working electrode (photoanode) was as follows: 20 mg of the sample was mixed with 2 mL ethyl alcohol to form a slurry and then coated onto a 1 cm × 1 cm fluorine-doped tin oxide (FTO) glass substrate and dried. The reactive species in the photocatalysis were investigated by the electron spin resonance test using the X-band (9.45 GHZ) with 5.00 G modulation amplitude and a magnetic field modulation of 100 kHz. The contact angles of H_2O drops deposited on the surface of the film were measured at 25 °C using a contact angle meter (SL150, Kino Industrial Co., Ltd., Shanghai, China).

2.3. Photocatalytic Performance

In a typical process, 20 mg photocatalyst and 100 mL MB solution (10 mg L^{-1}) as a standard pollutant were mixed in a 250 mL reaction vessel with a recirculating cooling water system at 25 °C under simulated solar light irradiation. Prior to the photocatalysis experiment, the sample solution was stirred for 60 min in the dark. The suspension was then exposed to a 300 W xenon lamp light equipped with a UV cutoff filter ($\lambda > 420$ nm) under continuous magnetic stirring. At given time intervals, 3 mL suspension from the reaction vessel was pipetted and centrifuged to separate the photocatalyst powder and MB solution. Finally, the absorption spectrum of the supernatant was determined by a UV–Vis spectrophotometer and the absorbance of MB was measured at 665 nm. The degradation efficiency of MB was calculated by the following equation:

$$\text{Degradation efficiency of MB (\%)} = (C_0 - C_t)/C_0 \times 100\%.$$

where C_0 and C_t represent the initial concentration of MB before irradiation and the residual concentration of MB in solution at irradiation time t, respectively.

3. Results and Discussion

3.1. The Morphology and Structure Characterization of the Catalysts

The crystal structures of CeO_2, Sm–CeO_2, Vo–CeO_2, and Vo–Sm–CeO_2 were first identified by X-ray diffraction (XRD). As described in Figure 1b, the peaks of all the prepared samples could be indexed to the (111), (200), (220), (311), (222) planes of the typical cubic structure of CeO_2 (JCPD#34-0394) [34]. No other new peaks appeared for Sm–CeO_2 and the Vo–Sm–CeO_2 samples, suggesting that Sm_2O_3 was

not produced, while the footprints of Sm could be detected by the X-ray photoelectron spectroscopy (XPS) (Figure 1c). The Sm 3d peaks were located at 1084 eV and 1110 eV, suggesting the existent of Sm^{3+} [45]. Combined with the XRD results, it confirms that Sm was doped into the Sm–CeO_2 and Vo–Sm–CeO_2 samples.

The morphology of the prepared samples was observed by scanning electron microscopy (SEM) and transmission electron microscopy (TEM). Figure S1 demonstrates the SEM images of CeO_2, Sm–CeO_2, Vo–CeO_2, and Vo–Sm–CeO_2. Four samples demonstrated almost the same morphology of nanorods, suggesting that doping and introduction of defects did not change the morphology and that the specific surface areas did not have much difference (Figure S2). Moreover, Figure 2a shows the TEM image of Vo–Sm–CeO_2. Nanorod morphology could be seen and the inset selected area electron diffraction (SAED) pattern demonstrated that it was polycrystalline. High resolution transmission electron microscopy (HRTEM) of pristine CeO_2 and Vo–Sm–CeO_2 is provided for contrast (Figure 2b,c). Pristine CeO_2 demonstrates the well-lined 0.156 nm lattice spacing, which is in accordance with (222) CeO_2 [34]. Significantly, the inside lattice spacing of Vo–Sm–CeO_2 became disordered, suggesting that numerous defects are generated after doping Sm. Closer inspection using high-angle annular dark-field scanning TEM (HAADF-TEM) showed the nanorod morphology of Vo–Sm–CeO_2 (Figure 2d). High multiples of the images of Vo–Sm–CeO_2 demonstrated that there was an obvious distortion atom, which may originate from Sm doping [46]. Furthermore, the corresponding EDX mapping (Figure 2g) indicated that Ce and Sm were homogeneously distributed in the Vo–Sm–CeO_2 nanorods.

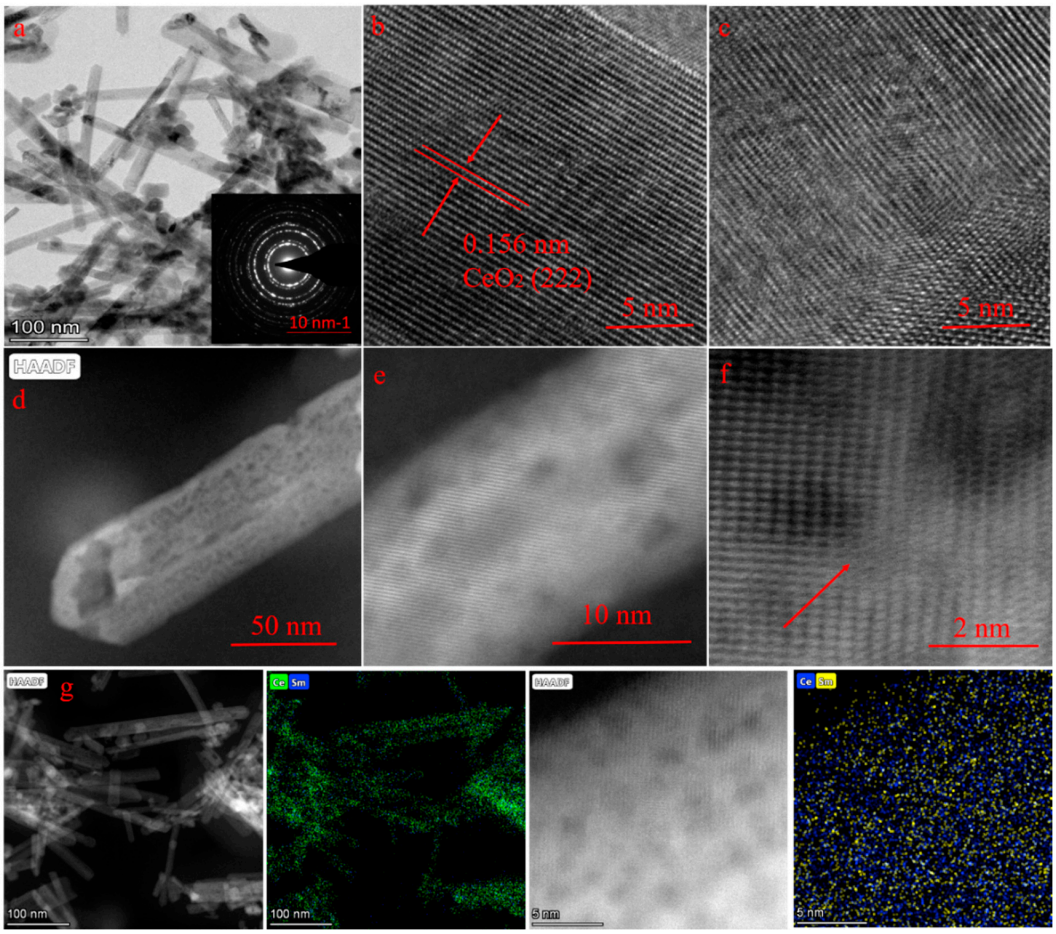

Figure 2. (**a**) Transmission electron microscope (TEM) images of Vo–Sm–CeO_2, high resolution transmission electron microscopy (HR-TEM) of (**b**) CeO_2, and (**c**) Vo–Sm–CeO_2, (**d**–**f**) high-angle annular dark-field scanning TEM (HAADF-STEM) mages of Vo–Sm–CeO_2, (**g**) energy dispersive X-ray spectroscopy (EDS) images of Vo–Sm–CeO_2.

The existence of defects was confirmed by XPS, Raman, and electron spin resonance spectroscopy [47,48]. Figure 3a shows the O 1s XPS of all samples. Two strong peaks appeared at 529.1 eV and 531.3 eV for pristine CeO_2 nanorods, which were indexed to lattice oxygen and surface active oxygen [49]. The lattice oxygen peak of Vo–Sm–CeO_2 shifted 0.3 eV toward low energy due to the effect of Sm doping and the intensity of the surface active oxygen peak increased, suggesting the existence of more surface defects. The surface property of the four samples was detected by the contact angles with the water droplet (Figure 3b). The contact angles decreased after Sm doping and introducing defects, suggesting that Vo–Sm–CeO_2 was in better contact with water. Furthermore, the Raman spectra of the four samples demonstrated the existence of defects (Figure 3c). The peak at 465 cm^{-1} can be indexed to the vibrational mode of fluorite-type CeO_2 and the peak at 600 cm^{-1} was attributed to the defects [50]. Figure 3d describes the EPR image of CeO_2, Sm–CeO_2, Vo–CeO_2, and Vo–Sm–CeO_2. No obvious signal was detected in the pristine CeO_2 nanorods, while Sm–CeO_2 and Vo–Sm–CeO_2 demonstrated a characteristic peak of defect, confirming the approach to creating defective materials [47].

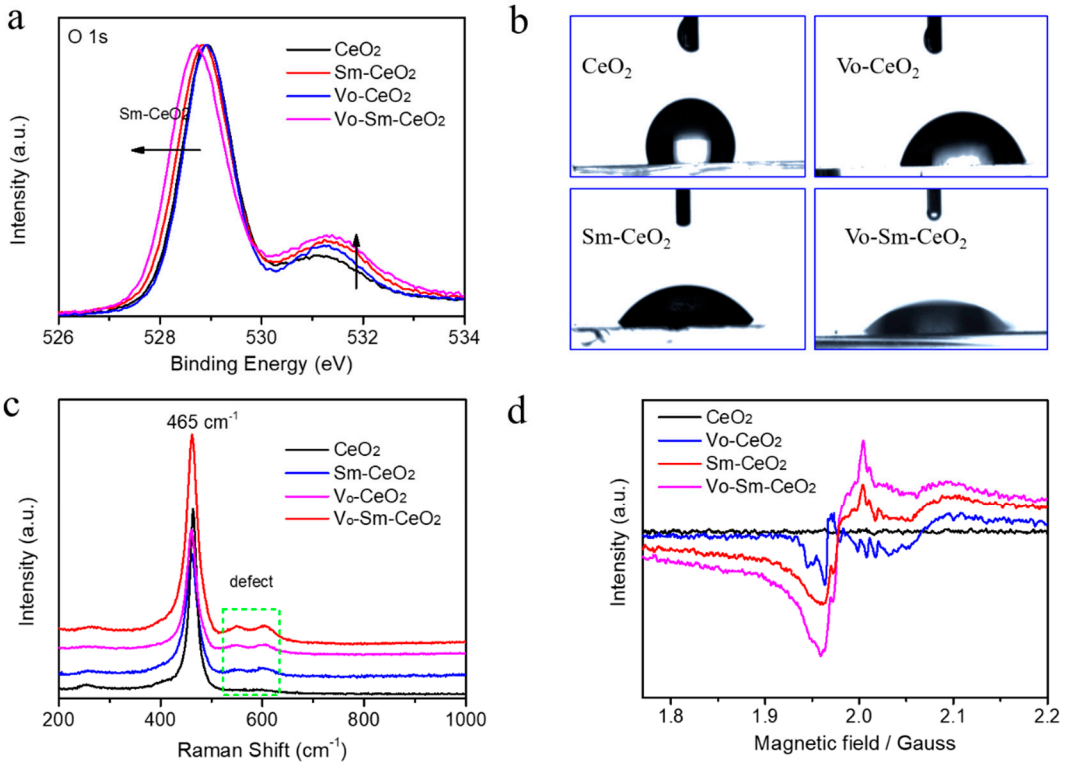

Figure 3. (**a**) O 1s XPS spectra. (**b**) Contact angles with water droplet, (**c**) Raman spectra, and (**d**) EPR spectra of CeO_2, Sm–CeO_2, Vo–CeO_2, and Vo–Sm–CeO_2.

3.2. Photocatalytic Performance of the Catalysts

To study the relationship between Sm doping and defects with photocatalytic performance, CeO_2, Sm–CeO_2, Vo–CeO_2, and Vo–Sm–CeO_2 were used to remove the MB with a 300 W xenon lamp irradiation. Figure 4a shows the photodegradation efficiencies of the four samples. Obviously, the photolysis of MB without photocatalysts can be ignored under our experimental conditions. Pristine CeO_2 nanorods had 40% photodegradation efficiency after 2 h irradiation. Significantly, Sm doping and defects can enhance the photocatalytic performance of CeO_2. Sm–CeO_2 and Vo–CeO_2 possessed 85% and 80% photodegradation efficiencies, respectively. The Vo–Sm–CeO_2 sample demonstrated the best degradation performance among the four samples, which could almost entirely remove the MB at 90 min irradiation. The doping amount of Sm was also optimized, which is shown in Figure S3. This result suggests that Sm-doping and surface defects co-promote the photocatalytic

activity of CeO_2. Furthermore, Figure 4b displays the reaction kinetic of photodegradation MB based on Figure 4a, which can be indexed to the Langmuir–Hinshelwood first-order kinetics model. The rate constant value of the Vo–Sm–CeO_2 sample was 0.012 min^{-1}, which was much higher than those of CeO_2 (0.003 min^{-1}), Sm-CeO_2 (0.007 min^{-1}), and Vo-CeO_2 (0.007 min^{-1}). The performance of Vo–Sm–CeO_2 was also compared with other reported Ce based photocatalysts (Table S1), suggesting that the Vo–Sm–CeO_2 sample had a superior photocatalytic performance. Furthermore, the total organic carbon (TOC) removal was performed to identify that the MB removal could be attributed to mineralization. The TOC removal efficiencies (120 min) for MB of CeO_2, Vo–CeO_2, Sm–CeO_2, and Vo–Sm–CeO_2 samples were 35%, 79%, 75%, and 98%, respectively (Figure S4). This result revealed that most of the MB were mineralized to H_2O and CO_2 during our degradation condition.

Photocatalytic stability is an important factor for the application of photocatalysts [51]. Figure 4c depicts the cycling stability of Vo–Sm–CeO_2 nanorods under visible light irradiation. After five cycles of testing, the photodegradation efficiency of Vo–Sm–CeO_2 nanorods reduced to 85% and the morphology and the crystal structures remained the same (Figure S4). Defects on the Vo–Sm–CeO_2 surface of the nanorods can be refilled with oxygen gas, which then affects its stability, as can be observed in other reports. Therefore, we used Vo–Sm–CeO_2 nanorods to anneal in air and test its performance. Just as we expected, the performance decreased, similar to the performance of the Sm–CeO_2 nanorods. Interestingly, the degradation efficiency could reach 99% after re-calcining in nitrogen, suggesting that defects can also regenerate on the surface of the Vo–Sm–CeO_2 nanorods (Figure 4d).

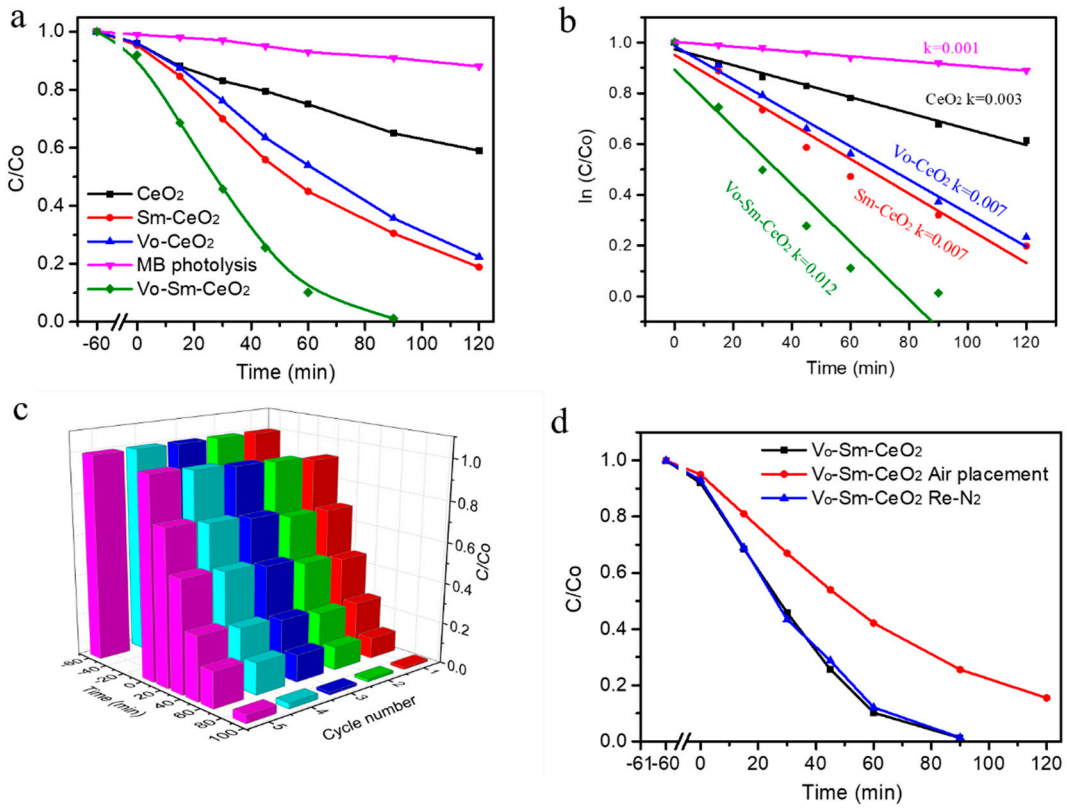

Figure 4. (**a**) Photocatalytic performance of the degradation of MB, (**b**) reaction kinetic, (**c**) stability test toward CeO_2, Sm–CeO_2, Vo–CeO_2, and Vo–Sm–CeO_2. (**d**) Photocatalytic performance of Vo-Sm-CeO_2 after treatment.

3.3. Active Species Trapping Experiments

Active species such as superoxide radicals, hydroxyl radicals, and h^+ play an important role in advanced oxidation processes (AOPS) technology [52]. To understand which active species generated

during the photocatalytic oxidation reaction, we performed active species trapping experiments and electron spin resonance (ESR) measurements [4,34]. Figure 5a shows the photodegradation efficiency of Vo–Sm–CeO_2 nanorods with different scavengers after 90 min irradiation with visible light (benzoquinone for O_2^-, ter-butyl alcohol for OH, and methanol for h^+). Obviously, the photodegradation efficiencies decreased after adding three scavengers, suggesting that O_2^-, OH, and h^+ are generated during photocatalysis. The active species have a high oxidizing ability to degrade MB into small molecules. Furthermore, Figure 5b,c displays the ESR results of DMPO-·OH and DMPO-O_2^- for Vo–Sm–CeO_2 nanorods using 5,5-dimethyl-1-pyrriline noxide (DMPO) as a spin trap. No signal corresponding to DMPO-·OH and DMPO-·O_2^- were detected for Vo–Sm–CeO_2 nanorods in the dark, suggesting ROS did not generated without light irradiation. Four strong peaks were observed when the light was turned on, which was indexed to DMPO-·OH [4,34] and six peaks corresponding to DMPO-O_2^- appeared, suggesting that ·O_2^- was produced during the photocatalysis [30]. The ESR results were consistent with the active species trapping experiments, suggesting that O_2^-, OH, and H^+ play an extremely important role in photocatalysis.

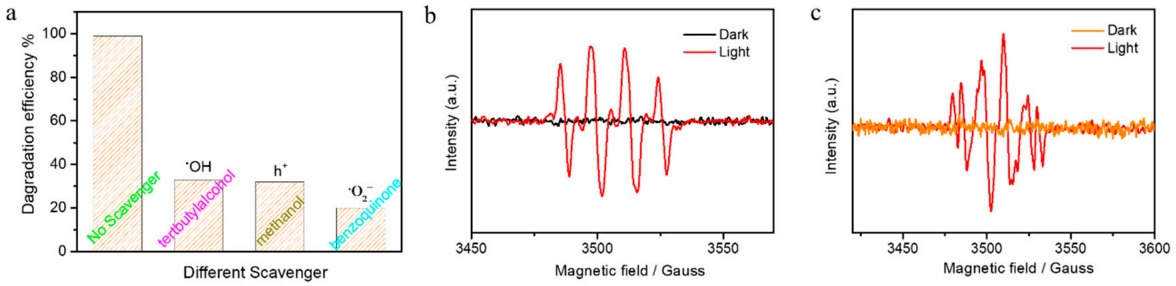

Figure 5. (**a**) Photodegradation efficiency of Vo–Sm–CeO_2 nanorods with different scavengers after 90 min. The ESR results of the Vo–Sm–CeO_2 nanorods: (**b**) DMPO-OH and (**c**) DMPO-O_2^-.

3.4. Charge Transfer Analysis

To study the effect of defects and Sm doping in CeO_2 nanorods, several characterizations were performed including transient photocurrent responses and electrochemical impedance spectra (ZIS) [53–55]. Figure 6a shows the transient photocurrent responses of the four samples. The current density value of Vo–Sm–CeO_2 was higher than those of CeO_2, Sm–CeO_2, and Vo–CeO_2 in the same window, suggesting that Vo–Sm–CeO_2 had the fast charge transfer. Note that the values of Vo–CeO_2 and Vo–Sm–CeO_2 decreased after several ON–OFF cycles, which was in accordance with the stability. Furthermore, the charge behaviors were analyzed by ZIS spectra under visible light irradiation (Figure 6b) [56]. Vo–Sm–CeO_2 displayed the smallest dimeter among the four samples, suggesting that it had a small charge transfer resistance [57]. The charge transfer resistance value of Sm–CeO_2 was smaller than that of Vo–CeO_2, suggesting that Sm doping mainly improved the conductivity of CeO_2 [58]. Therefore, Sm doping and defects can improve the charge transfer of CeO_2.

The light absorption range of CeO_2, Sm–CeO_2, Vo–CeO_2, and Vo–Sm–CeO_2 was observed by UV-Vis spectra (Figure 6c). It can be seen that pristine CeO_2 nanorods had an absorption region at 420 nm, suggesting that it responds to UV light. After Sm doping and introducing defects into CeO_2, the absorption band gap displayed little blue shift, suggesting that light absorption was not the main effect for the photocatalytic performance. The bandgaps of four samples could be calculated based on the following formula: $a = A(hv - Eg)^2/hv$ (a is the absorption coefficient and A is the absorption constant for indirect transition) [59,60]. Therefore, the bandgap values of CeO_2, Sm–CeO_2, Vo–CeO_2, and Vo–Sm–CeO_2 were 2.55 eV, 2.48 eV. 2.75 eV, and 2.51 eV, respectively. Interestingly, Sm doping could narrow the bandgap while defects increased the bandgap [61–63]. The relative valence band maximum (VBM) value could be obtained by the XPS valence spectra (Figure 6e). The VBM values of pristine CeO_2 and Vo–Sm–CeO_2 were about 1.93 and 1.56 eV, respectively. The schematic for the proposed mechanism is shown in Figure 6f. Doping Sm into the CeO_2 nanorods changed the

location of VBM and CBM, and enhanced the electrical conductivity. Photoelectrons in the CBM of Vo–Sm–CeO_2 are more conductive to producing reactive oxygen species due to its high potential of CBM. Furthermore, defects on the surface of the Vo–Sm–CeO_2 nanorods can act as reactor sites for O_2 reduction. All these results enable Vo–Sm–CeO_2 nanorods to have better photocatalytic performance.

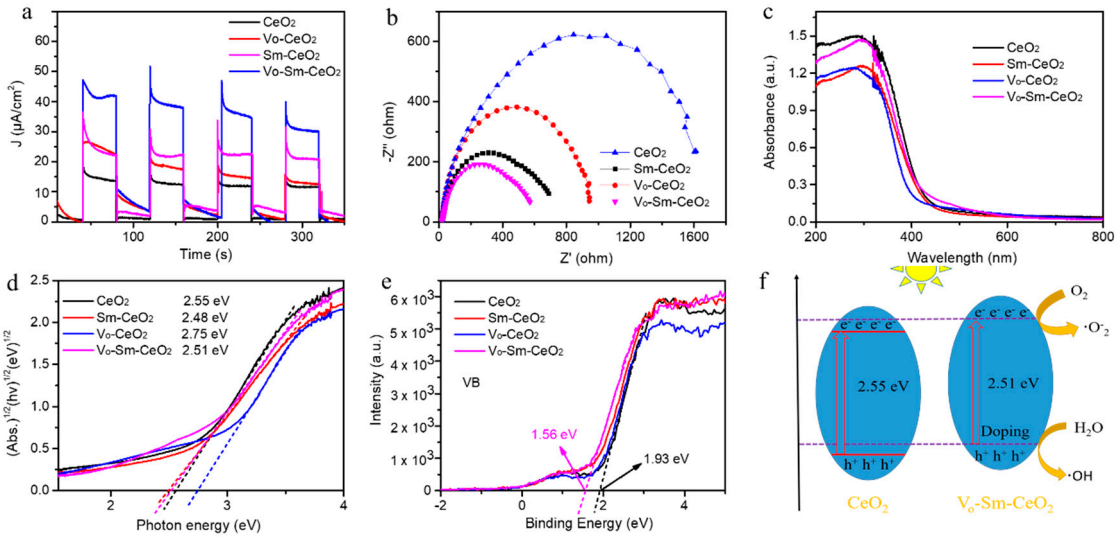

Figure 6. (**a**) Transient photocurrent responses, (**b**) electrochemical impedance spectra (applied potential 0.1 eV), (**c**) UV–Vis spectra, (**d**) optical band gaps, (**e**) VB spectra from XPS of CeO_2, Sm–CeO_2, Vo–CeO_2, and Vo–Sm–CeO_2. (**f**) Schematic for the proposed mechanism.

4. Conclusions

In this work, we report on a defective Sm–CeO_2 nanorod photocatalyst that had a superior photodegradation performance of MB (almost 100%, 90 min) under visible light irradiation. Such performance was achieved due to the synergistic effect of defects and Sm doping, which enhanced the separation of the photogenerated holes and electrons. Sm doping can effectively improve the conductivity of CeO_2 nanorods and the surface defects can act as reactive sites for photogenerated electrons to reduce O_2 into $\cdot O_2^-$. This work not only provides a better understanding of the photocatalytic mechanism, but also offers some guidance for designing a Ce based photocatalyst with high efficient performance.

Supplementary Materials: The following are available online at http://www.mdpi.com/2079-4991/10/11/2307/s1, Figure S1: SEM images of CeO_2, Sm–CeO_2, Vo–CeO_2, and Vo–Sm–CeO_2; Figure S2: The N_2 adsorption spectra of all samples; Figure S3: Photocatalytic performance of Sm doping CeO_2; Figure S4: TOC removal efficiency CeO_2, Sm–CeO_2, Vo–CeO_2, and Vo–Sm–CeO_2 at 120 min; Figure S5: XRD spectra and SEM image of Vo–Sm–CeO_2 after the five cycles test; Table S1: The performance of Vo–Sm–CeO_2 was also compared with other reported Ce based photocatalysts.

Author Contributions: J.Y. performed the experiments and wrote the paper; N.X., J.Z. and W.F. partly performed the experiments; Y.H. designed and reviewed the manuscript; Y.T. conceived, designed, and provided the equipment. All authors have read and agreed to the published version of the manuscript.

Funding: This work was supported by the Natural Science Foundation of China (21706295 and 21773315), the Natural Science Foundation of Guangdong Province (2020A1515010798), the Pearl River S & T Nova Program of Guangzhou (201906010024), the Local Innovative and Research Teams Project of Guangdong Pearl River Talents Program (2017BT01C102), the Science and Technology Research Project of Guangzhou (202002010007), the Special Fund for Science and Technology Innovation Strategy of Guangdong Province (pdjh2020b0468), and the Guangzhou University national college students' innovation and entrepreneurship training program (202011078020).

Conflicts of Interest: The authors declare no conflict of interest.

References

1. Yin, H.; Li, G.; Chen, X.; Wang, W.; Wong, P.K.; Zhao, H.; An, T. Accelerated evolution of bacterial antibiotic resistance through early emerged stress responses driven by photocatalytic oxidation. *Appl. Catal. B Environ.* **2020**, *269*, 118829. [CrossRef]
2. Martin, D.J.; Liu, G.; Moniz, S.J.A.; Bi, Y.; Beale, A.M.; Ye, J.; Tang, J. Efficient visible driven photocatalyst, silver phosphate: Performance, understanding and perspective. *Chem. Soc. Rev.* **2015**, *44*, 7808–7828. [CrossRef] [PubMed]
3. Di, J.; Xiong, J.; Li, H.; Liu, Z. Ultrathin 2D photocatalysts: Electronic-structure tailoring, hybridization, and applications. *Adv. Mater.* **2018**, *30*, 1704548. [CrossRef] [PubMed]
4. Huang, Y.; Guo, Z.; Liu, H.; Zhang, S.; Wang, P.; Lu, J.; Tong, Y. Heterojunction architecture of N-Doped WO_3 nanobundles with Ce_2S_3 nanodots hybridized on a carbon textile enables a highly efficient flexible photocatalyst. *Adv. Funct. Mater.* **2019**, *29*, 1903490. [CrossRef]
5. He, R.; Xu, D.; Cheng, B.; Yu, J.; Ho, W. Review on nanoscale Bi-based photocatalysts. *Nanoscale Horiz.* **2018**, *3*, 464–504. [CrossRef] [PubMed]
6. Wang, W.; Li, G.; Xia, D.; An, T.; Zhao, H.; Wong, P.K. Photocatalytic nanomaterials for solar-driven bacterial inactivation: Recent progress and challenges. *Environ. Sci. Nano* **2017**, *4*, 782–799. [CrossRef]
7. Bertagna Silva, D.; Cruz-Alcalde, A.; Sans, C.; Giménez, J.; Esplugas, S. Performance and kinetic modelling of photolytic and photocatalytic ozonation for enhanced micropollutants removal in municipal wastewaters. *Appl. Catal. B Environ.* **2019**, *249*, 211–217. [CrossRef]
8. Habibi-Yangjeh, A.; Asadzadeh-Khaneghah, S.; Feizpoor, S.; Rouhi, A. Review on heterogeneous photocatalytic disinfection of waterborne, airborne, and foodborne viruses: Can we win against pathogenic viruses? *J. Colloid Interface Sci.* **2020**, *580*, 503–514. [CrossRef]
9. Zhang, W.; Li, G.; Liu, H.; Chen, J.; Ma, S.; Wen, M.; Kong, J.; An, T. Photocatalytic degradation mechanism of gaseous styrene over Au/TiO_2@CNTs: Relevance of superficial state with deactivation mechanism. *Appl. Catal. B Environ.* **2020**, *272*, 118969. [CrossRef]
10. Sapkota, K.P.; Lee, I.; Abu Hanif, M.; Islam, M.A.; Hahn, J.R. Solar-light-driven efficient ZnO-single-Walled carbon nanotube photocatalyst for the degradation of a persistent water pollutant organic dye. *Catalysts* **2019**, *9*, 498. [CrossRef]
11. Cahino, A.M.; Loureiro, R.G.; Dantas, J.; Madeira, V.S.; Ribeiro Fernandes, P.C. Characterization and evaluation of ZnO/CuO catalyst in the degradation of methylene blue using solar radiation. *Ceram. Int.* **2019**, *45*, 13628–13636. [CrossRef]
12. Li, K.; Lu, X.; Zhang, Y.; Liu, K.; Huang, Y.; Liu, H. Bi_3TaO_7/Ti_3C_2 heterojunctions for enhanced photocatalytic removal of water-borne contaminants. *Environ. Res.* **2020**, *185*, 109409. [CrossRef] [PubMed]
13. Su, T.; Shao, Q.; Qin, Z.; Guo, Z.; Wu, Z. Role of interfaces in two-dimensional photocatalyst for water splitting. *ACS Catal.* **2018**, *8*, 2253–2276. [CrossRef]
14. Su, T.; Hood, Z.D.; Naguib, M.; Bai, L.; Luo, S.; Rouleau, C.M.; Ivanov, I.N.; Ji, H.; Qin, Z.; Wu, Z. Monolayer $Ti_3C_2T_x$ as an effective co-catalyst for enhanced photocatalytic hydrogen production over TiO_2. *ACS Appl. Energy Mater.* **2019**, *2*, 4640–4651. [CrossRef]
15. Huang, H.; Pradhan, B.; Hofkens, J.; Roeffaers, M.B.J.; Steele, J.A. Solar-driven metal halide perovskite photocatalysis: Design, stability, and performance. *ACS Energy Lett.* **2020**, *5*, 1107–1123. [CrossRef]
16. Lv, Y.; Liu, Y.; Zhu, Y.; Zhu, Y. Surface oxygen vacancy induced photocatalytic performance enhancement of a $BiPO_4$ nanorod. *J. Mater. Chem. A* **2014**, *2*, 1174–1182. [CrossRef]
17. Zhu, Y.; Ling, Q.; Liu, Y.; Wang, H.; Zhu, Y. Photocatalytic performance of $BiPO_4$ nanorods adjusted via defects. *Appl. Catal. B Environ.* **2016**, *187*, 204–211. [CrossRef]
18. Zhang, N.; Li, X.; Ye, H.; Chen, S.; Ju, H.; Liu, D.; Lin, Y.; Ye, W.; Wang, C.; Xu, Q.; et al. Oxide defect engineering enables to couple solar energy into oxygen activation. *J. Am. Chem. Soc.* **2016**, *138*, 8928–8935. [CrossRef]
19. Wu, J.; Li, X.; Shi, W.; Ling, P.; Sun, Y.; Jiao, X.; Gao, S.; Liang, L.; Xu, J.; Yan, W.; et al. Efficient visible-light-driven CO_2 reduction mediated by defect-engineered BiOBr atomic layers. *Angew. Chem. Int. Edit.* **2018**, *57*, 8719–8723. [CrossRef]

20. Yang, X.; Wang, S.; Yang, N.; Zhou, W.; Wang, P.; Jiang, K.; Li, S.; Song, H.; Ding, X.; Chen, H.; et al. Oxygen vacancies induced special CO_2 adsorption modes on Bi_2MoO_6 for highly selective conversion to CH_4. *Appl. Catal. B Environ.* **2019**, *259*, 118088. [CrossRef]
21. Xie, C.; Yan, D.; Li, H.; Du, S.; Chen, W.; Wang, Y.; Zou, Y.; Chen, R.; Wang, S. Defect chemistry in heterogeneous catalysis: Recognition, understanding and utilization. *ACS Catal.* **2020**, *10*, 11082–11098. [CrossRef]
22. Wang, H.; Zhang, W.; Li, X.; Li, J.; Cen, W.; Li, Q.; Dong, F. Highly enhanced visible light photocatalysis and in situ FT-IR studies on Bi metal@defective BiOCl hierarchical microspheres. *Appl. Catal. B Environ.* **2018**, *225*, 218–227. [CrossRef]
23. Zhang, Y.; Xu, Z.; Li, G.; Huang, X.; Hao, W.; Bi, Y. Direct observation of oxygen vacancy self-healing on TiO_2 photocatalysts for solar water splitting. *Angew. Chem.* **2019**, *58*, 14229–14233. [CrossRef]
24. Wang, S.; He, T.; Chen, P.; Du, A.; Ostrikov, K.; Huang, W.; Wang, L. In situ formation of oxygen vacancies achieving near-complete charge separation in planar $BiVO_4$ photoanodes. *Adv. Mater.* **2020**, *32*, 2001385. [CrossRef] [PubMed]
25. Di, J.; Xia, J.; Chisholm, M.F.; Zhong, J.; Chen, C.; Cao, X.; Dong, F.; Chi, Z.; Chen, H.; Weng, Y.-X.; et al. Defect-tailoring mediated electron–hole separation in single-unit-cell Bi_3O_4Br nanosheets for boosting photocatalytic hydrogen evolution and nitrogen fixation. *Adv. Mater.* **2019**, *31*, 1807576. [CrossRef]
26. Yu, H.; Li, J.; Zhang, Y.; Yang, S.; Han, K.; Dong, F.; Ma, T. Three-in-one oxygen vacancies: Whole visible-spectrum absorption, efficient charge separation, and surface site activation for robust CO_2 photoreduction. *Angew. Chem.* **2019**, *58*, 3880–3884. [CrossRef]
27. Selim, S.; Pastor, E.; García-Tecedor, M.; Morris, M.R.; Francàs, L.; Sachs, M.; Moss, B.; Corby, S.; Mesa, C.A.; Gimenez, S.; et al. Impact of oxygen vacancy occupancy on charge carrier dynamics in $BiVO_4$ photoanodes. *J. Am. Chem. Soc.* **2019**, *141*, 18791–18798. [CrossRef]
28. Liu, D.; Wang, C.; Yu, Y.; Zhao, B.-H.; Wang, W.; Du, Y.; Zhang, B. Understanding the nature of ammonia treatment to synthesize oxygen vacancy-enriched transition metal oxides. *Chem* **2019**, *5*, 376–389. [CrossRef]
29. Glass, D.; Cortés, E.; Ben-Jaber, S.; Brick, T.; Peveler, W.J.; Blackman, C.S.; Howle, C.R.; Quesada-Cabrera, R.; Parkin, I.P.; Maier, S.A. Dynamics of photo-induced surface oxygen vacancies in metal-oxide semiconductors studied under ambient conditions. *Adv. Sci.* **2019**, *6*, 1901841. [CrossRef]
30. Dong, F.; Xiong, T.; Sun, Y.; Huang, H.; Wu, Z. Synergistic integration of thermocatalysis and photocatalysis on black defective $(BiO)_2CO_3$ microspheres. *J. Mater. Chem. A* **2015**, *3*, 18466–18474. [CrossRef]
31. Yu, S.; Zhang, Y.; Dong, F.; Li, M.; Zhang, T.; Huang, H. Readily achieving concentration-tunable oxygen vacancies in $Bi_2O_2CO_3$: Triple-functional role for efficient visible-light photocatalytic redox performance. *Appl. Catal. B Environ.* **2018**, *226*, 441–450. [CrossRef]
32. Kong, J.; Xiang, Z.; Li, G.; An, T. Introduce oxygen vacancies into CeO_2 catalyst for enhanced coke resistance during photothermocatalytic oxidation of typical VOCs. *Appl. Catal. B Environ.* **2020**, *269*, 118755. [CrossRef]
33. Ye, K.; Li, Y.; Yang, H.; Li, M.; Huang, Y.; Zhang, S.; Ji, H. An ultrathin carbon layer activated CeO_2 heterojunction nanorods for photocatalytic degradation of organic pollutants. *Appl. Catal. B Environ.* **2019**, *259*, 118085. [CrossRef]
34. Huang, Y.; Lu, Y.; Lin, Y.; Mao, Y.; Ouyang, G.; Liu, H.; Zhang, S.; Tong, Y. Cerium-based hybrid nanorods for synergetic photo-thermocatalytic degradation of organic pollutants. *J. Mater. Chem. A* **2018**, *6*, 24740–24747. [CrossRef]
35. Yan, Z.; Xu, Z.; Yu, J.; Jaroniec, M. Enhanced formaldehyde oxidation on CeO_2/AlOOH-supported Pt catalyst at room temperature. *Appl. Catal. B Environ.* **2016**, *199*, 458–465. [CrossRef]
36. Yang, H.; Xu, B.; Yuan, S.; Zhang, Q.; Zhang, M.; Ohno, T. Synthesis of Y-doped CeO_2/PCN nanocomposited photocatalyst with promoted photoredox performance. *Appl. Catal. B Environ.* **2019**, *243*, 513–521. [CrossRef]
37. Ma, Y.; Ou, P.; Wang, Z.; Zhu, A.; Lu, L.; Zhang, Y.; Zeng, W.; Song, J.; Pan, J. Interface engineering in CeO_2 (111) facets decorated with CdSe quantum dots for photocatalytic hydrogen evolution. *J. Colloid Interface Sci.* **2020**, *579*, 707–713. [CrossRef]
38. Qiu, B.; Wang, C.; Zhang, N.; Cai, L.; Xiong, Y.; Chai, Y. CeO_2-induced interfacial Co^{2+} octahedral sites and oxygen vacancies for water oxidation. *ACS Catal.* **2019**, *9*, 6484–6490. [CrossRef]
39. Jiang, D.; Wang, W.; Zhang, L.; Zheng, Y.; Wang, Z. Insights into the surface-defect dependence of photoreactivity over CeO_2 nanocrystals with well-defined crystal facets. *ACS Catal.* **2015**, *5*, 4851–4858. [CrossRef]

40. Aslam, M.; Qamar, M.T.; Soomro, M.T.; Ismail, I.M.I.; Salah, N.; Almeelbi, T.; Gondal, M.A.; Hameed, A. The effect of sunlight induced surface defects on the photocatalytic activity of nanosized CeO_2 for the degradation of phenol and its derivatives. *Appl. Catal. B Environ.* **2016**, *180*, 391–402. [CrossRef]
41. Huang, Y.; Long, B.; Tang, M.; Rui, Z.; Balogun, M.-S.; Tong, Y.; Ji, H. Bifunctional catalytic material: An ultrastable and high-performance surface defect CeO_2 nanosheets for formaldehyde thermal oxidation and photocatalytic oxidation. *Appl. Catal. B Environ.* **2016**, *181*, 779–787. [CrossRef]
42. Subramanyam, K.; Sreelekha, N.; Reddy, D.A.; Ramanadha, M.; Poornaprakash, B.; Reddy, K.C.; Vijayalakshmi, R.P. Influence of transition metals co-doping on CeO_2 magnetic and photocatalytic activities. *Ceram. Int.* **2020**, *46*, 5086–5097. [CrossRef]
43. Zheng, N.-C.; Ouyang, T.; Chen, Y.; Wang, Z.; Chen, D.-Y.; Liu, Z.-Q. Ultrathin CdS shell-sensitized hollow S-doped CeO_2 spheres for efficient visible-light photocatalysis. *Catal. Sci. Technol.* **2019**, *9*, 1357–1364. [CrossRef]
44. Laberty-Robert, C.; Long, J.W.; Pettigrew, K.A.; Stroud, R.M.; Rolison, D.R. Ionic nanowires at 600 °C: Using nanoarchitecture to optimize electrical transport in nanocrystalline gadolinium-doped ceria. *Adv. Mater.* **2007**, *19*, 1734–1739. [CrossRef]
45. Cheng, Y.; Nan, H.; Li, Q.; Luo, Y.; Chu, K. A rare-earth samarium oxide catalyst for electrocatalytic nitrogen reduction to ammonia. *ACS Sustain. Chem. Eng.* **2020**, *8*, 13908–13914. [CrossRef]
46. Liyanage, A.D.; Perera, S.D.; Tan, K.; Chabal, Y.; Balkus, K.J. Synthesis, characterization, and photocatalytic activity of Y-doped CeO_2 nanorods. *ACS Catal.* **2014**, *4*, 577–584. [CrossRef]
47. Ye, K.; Li, K.; Lu, Y.; Guo, Z.; Ni, N.; Liu, H.; Huang, Y.; Ji, H.; Wang, P. An overview of advanced methods for the characterization of oxygen vacancies in materials. *TrAC Trends Anal. Chem.* **2019**, *116*, 102–108. [CrossRef]
48. Liang, M.; Borjigin, T.; Zhang, Y.; Liu, B.; Liu, H.; Guo, H. Controlled assemble of hollow heterostructured g-C_3N_4@CeO_2 with rich oxygen vacancies for enhanced photocatalytic CO_2 reduction. *Appl. Catal. B Environ.* **2019**, *243*, 566–575. [CrossRef]
49. Huang, Y.; Li, K.; Lin, Y.; Tong, Y.; Liu, H. Enhanced efficiency of electron–hole separation in $Bi_2O_2CO_3$ for photocatalysis via acid treatment. *ChemCatChem* **2018**, *10*, 1982–1987. [CrossRef]
50. O'Neill, D.B.; Prezgot, D.; Ianoul, A.; Otto, C.; Mul, G.; Huijser, A. Silver nanocubes coated in ceria: Core/shell size effects on light-induced charge transfer. *ACS Appl. Mater. Interfaces* **2020**, *12*, 1905–1912. [CrossRef]
51. Luo, Y.; Wei, X.; Gao, B.; Zou, W.; Zheng, Y.; Yang, Y.; Zhang, Y.; Tong, Q.; Dong, L. Synergistic adsorption-photocatalysis processes of graphitic carbon nitrate (g-C_3N_4) for contaminant removal: Kinetics, models, and mechanisms. *Chem. Eng. J.* **2019**, *375*, 122019. [CrossRef]
52. Verma, N.; Ananthakrishnan, R. Riboflavin-immobilized CeO_2–RGO nanohybrid as a potential photoredox catalyst for enhanced removal of organic pollutants under visible light. *J. Phys. Chem. C* **2020**, *124*, 404–415. [CrossRef]
53. Shang, H.; Huang, S.; Li, H.; Li, M.; Zhao, S.; Wang, J.; Ai, Z.; Zhang, L. Dual-site activation enhanced photocatalytic removal of no with Au/CeO_2. *Chem. Eng. J.* **2020**, *386*, 124047. [CrossRef]
54. Wang, B.; Yang, S.-Z.; Chen, H.; Gao, Q.; Weng, Y.-X.; Zhu, W.; Liu, G.; Zhang, Y.; Ye, Y.; Zhu, H.; et al. Revealing the role of oxygen vacancies in bimetallic $PbBiO_2Br$ atomic layers for boosting photocatalytic CO_2 conversion. *Appl. Catal. B Environ.* **2020**, *277*, 119170. [CrossRef]
55. Balapure, A.; Ganesan, R. Anatase versus Triphasic TiO_2: Near-identical synthesis and comparative structure-sensitive photocatalytic degradation of methylene blue and 4-chlorophenol. *J. Colloid Interface Sci.* **2021**, *581*, 205–217. [CrossRef] [PubMed]
56. Hu, Y.; Xiong, T.; Balogun, M.S.J.T.; Huang, Y.; Adekoya, D.; Zhang, S.; Tong, Y. Enhanced metallicity boosts hydrogen evolution capability of dual-bimetallic Ni–Fe nitride nanoparticles. *Mater. Today Phys.* **2020**, *15*, 100267. [CrossRef]
57. Zhu, C.; Wang, Y.; Jiang, Z.; Xu, F.; Xian, Q.; Sun, C.; Tong, Q.; Zou, W.; Duan, X.; Wang, S. CeO_2 nanocrystal-modified layered MoS_2/g-C_3N_4 as 0D/2D ternary composite for visible-light photocatalytic hydrogen evolution: Interfacial consecutive multi-step electron transfer and enhanced H_2O reactant adsorption. *Appl. Catal. B Environ.* **2019**, *259*, 118072. [CrossRef]
58. Ye, K.-H.; Wang, Z.; Gu, J.; Xiao, S.; Yuan, Y.; Zhu, Y.; Zhang, Y.; Mai, W.; Yang, S. Carbon quantum dots as a visible light sensitizer to significantly increase the solar water splitting performance of bismuth vanadate photoanodes. *Energy Environ. Sci.* **2017**, *10*, 772–779. [CrossRef]

59. Yang, J.; Liang, Y.; Li, K.; Yang, G.; Yin, S. One-step low-temperature synthesis of 0D CeO_2 quantum dots/2D BiOX (X = Cl, Br) nanoplates heterojunctions for highly boosting photo-oxidation and reduction ability. *Appl. Catal. B Environ.* **2019**, *250*, 17–30. [CrossRef]
60. Song, H.; Wu, R.; Yang, J.; Dong, J.; Ji, G. Fabrication of CeO_2 nanoparticles decorated three-dimensional flower-like BiOI composites to build p-n heterojunction with highly enhanced visible-light photocatalytic performance. *J. Colloid Interface Sci.* **2018**, *512*, 325–334. [CrossRef]
61. Huang, Y.; Xu, H.; Yang, H.; Lin, Y.; Liu, H.; Tong, Y. Efficient charges separation using advanced BiOI-based hollow spheres decorated with palladium and manganese dioxide nanoparticles. *ACS Sustain. Chem. Eng.* **2018**, *6*, 2751–2757. [CrossRef]
62. Li, Y.; Liu, K.; Zhang, J.; Yang, J.; Huang, Y.; Tong, Y. Engineering the band-edge of Fe_2O_3/ZnO nanoplates via separate dual cation incorporation for efficient photocatalytic performance. *Ind. Eng. Chem. Res.* **2020**, *59*, 18865–18872. [CrossRef]
63. Li, Y.; Xia, Y.; Liu, K.; Ye, K.; Wang, Q.; Zhang, S.; Huang, Y.; Liu, H. Constructing Fe-MOF-derived Z-scheme photocatalysts with enhanced charge transport: Nanointerface and carbon sheath synergistic effect. *ACS Appl. Mater. Interfaces* **2020**, *12*, 25494–25502. [CrossRef] [PubMed]